Shared-Receiver Battery Equalizer Based on Inductive Power Transfer and Bidirectional DC–DC Converter

Yinqin Liao, *Student Member, IEEE*, Xinzhi Zhang, Long Chen, *Student Member, IEEE*, Feiliang Li, Chunsheng Wang, *Member, IEEE*, Yuan Cao, *Member, IEEE*, and Yukun Hu, *Senior Member, IEEE*

***Abstract*—State-of-charge (SOC) balancing is essential for safe, reliable, and long-lived operation of battery energy storage systems. Conventional wired equalizers are hampered by permanent physical connections, limited flexibility, and heightened safety hazards. To address these limitations, an inductive power transfer (IPT)-based equalizer is introduced in this article, in which the single-inductor dc–dc converter's inductor is replaced by a transmitter coil to wirelessly transfer ripple energy for SOC balancing during both charging and discharging. In addition, a single receiver coil and switch matrix are employed, shared sequentially among all cells with adaptive connection intervals regulated by a presented efficient adaptive equalization algorithm. The equalization performance is analyzed and validated using a down-scaled proof-of-concept prototype. Furthermore, the trade-off between balancing capability and efficiency is discussed, along with the potential for cell-level fault bypass at a slight improvement in topology.**

***Index Terms*—Battery balancing, energy storage system, inductive power transfer (IPT), state-of-charge (SoC).**

I. Introduction

LITHIUM-ION batteries, as representatives of energy storage systems, are extensively employed in electric vehicles (EVs), smart grids, consumer electronics, and other applications due to their advantages of high energy density, long lifespan, and no memory effect etc. [1], [2], [3]. In general, lithium-ion battery cells are connected in series or parallel to meet high voltage or power requirements [4]. However, variations in charging and discharging rates can arise due to differences in fabrication parameters, state-of-health (SOH), and ambient temperature, leading to state-of-charge (SOC) imbalances [5]. These SOC discrepancies not only pose potential fire and explosion hazards during charging but can also cause irreversible battery damage during discharging, resulting in shortened battery lifespans [6].

Battery equalization is essential for prolonging the lifespan and improving the safety of series-connected lithium-ion cells. Numerous equalizer topologies have been developed and can be broadly categorized into passive and active approaches [7]. Passive methods are favored for their simplicity and low cost [8], but they dissipate excess energy as heat, leading to thermal management challenges. Active equalizers, on the other hand, redistribute charge among cells using external circuits based on switched capacitors [9], inductors [10], dc–dc converters [11], [12], transformers [13], [14], [15], [16], [17], [18] or wireless power transfer (WPT) [19], [20], [21], [22], [23], [24], [25], [26], [27].

Among these, transformer-based equalizers remain popular due to their high energy efficiency and electrical isolation. However, reliance on iron cores induces bulky designs, raises material costs, and introduces safety concerns such as core saturation, overheating, and fault risks [19], [23]. These core-related limitations motivate the exploration of WPT-based equalizers, which offer contactless, coreless energy transfer and thereby improve safety, flexibility, and modularity.

Recent WPT-based equalizers can be categorized into multireceiver and single-receiver architectures. Multireceiver systems, such as the megahertz-range design presented in [19], allow simultaneous balancing of multiple cells but require a full-bridge rectifier and a dedicated receiver (Rx) coil per cell, increasing component count and cost. To address this, Liu et al. [20] employ the voltage doublers, which reduce the number of required diodes and Rx coils by half. Further reduction is achieved in the modular equalizer proposed in [21], which minimizes the number of Rx coils under similar operating conditions as in [19]. In addition, a dual-layer receiver architecture in [22] enhanced antimisalignment capability in multireceiver systems. Nevertheless, cross-coupling between coils and inconsistent parameters of Rx coils can still degrade balancing performance [28].

To overcome these drawbacks, single-receiver architectures have been introduced. In [23], a voltage equalizer (VE) with a single Rx coil enables cell balancing during charging, but the

Received 23 June 2025; revised 5 August 2025; accepted 28 August 2025. Date of publication 1 September 2025; date of current version 23 December 2025. This work was supported in part by the National Natural Science Foundation (NNSF) of China under Grant 62103443, in part by the Hunan Natural Science Foundation under Grant 2022JJ40630, and in part by the Fundamental Research Funds for the Central Universities of Central South University under Grant 2025ZZTS0734. Recommended for publication by Associate Editor J. Lam. *(Corresponding author: Yuan Cao.)*

Yinqin Liao, Xinzhi Zhang, Long Chen, Feiliang Li, Chunsheng Wang, and Yuan Cao are with the School of Automation, Central South University, Changsha 410083, China (e-mail: liao_yinqin@csu.edu.cn; 244612238@csu.edu.cn; chend1729@csu.edu.cn; csu_xffl@csu.edu.cn; wang csu@csu.edu.cn; caoyuan3116@csu.edu.cn).

Yukun Hu is with the Department of Civil, Environment and Geomatic Engineering, University College London, WC1E 6BT London, U.K. (e-mail: yukun.hu@ucl.ac.uk).

Color versions of one or more figures in this article are available at https://doi.org/10.1109/TPEL.2025.3605072.

Digital Object Identifier 10.1109/TPEL.2025.3605072

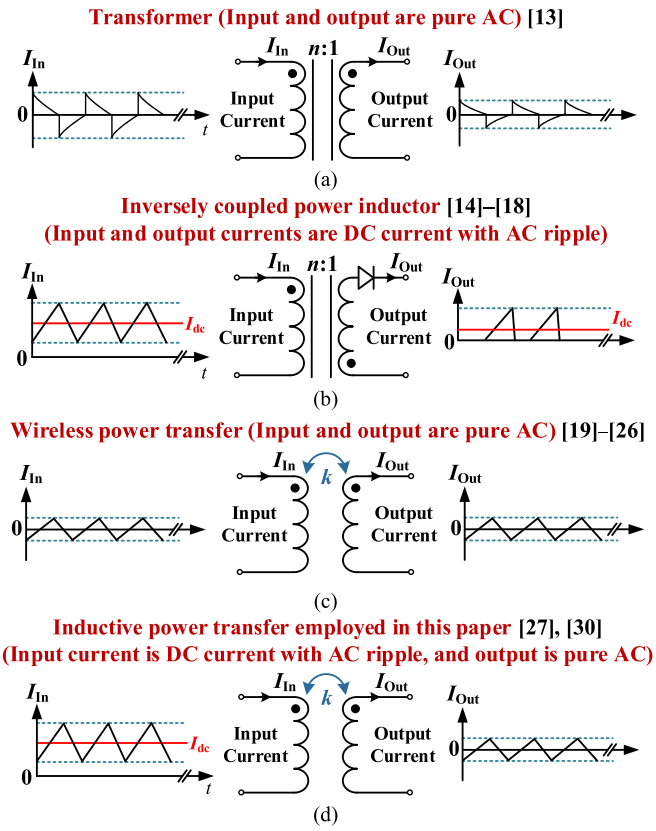

Fig. 1. Configurations and waveforms of different power transfer mechanisms. (a) Conventional transformer. (b) Coupled inductor (flyback converter). (c) WPT. (d) Employed IPT method.

integrated voltage multiplier (VM) topology suffers from low conversion efficiency [29]. To improve this, Zhang et al. [24] introduce a hybrid switching strategy that alternates between VE and a rectifier bridge to reduce conduction losses. Furthermore, switch-matrix-based designs in [25] achieve higher efficiency active balancing without relying on VM topologies.

Despite their advantages, most existing WPT-based battery equalizers are limited in operational flexibility. For instance, the work in [26] support balancing only during idle states, [19], [20], [21], [22], [23], [24], and [25] operate solely during charging due to their reliance on external ac sources or internal inverters, and [27] functions only during discharging by utilizing current ripple. Such single-direction operation allows SOC differences in the other mode to accumulate, leading to large deviations when switching between charging and discharging, which can destabilize balancing control and increase the risk of over-charge or over-discharge, potentially causing capacity loss, thermal runaway, or even safety failures [6].

To fill this gap, an inductive power transfer (IPT)-based equalizer capable of bidirectional balancing during charging and discharging is introduced in this work. Although both transformers and IPT systems utilize magnetic induction, their operating principles are completely different. To clarify these differences, Fig. 1 shows the configurations of a transformer method, a coupled inductors method, a classical WPT system, and the IPT method employed in this work.

In Fig. 1(a), the conventional transformer consists of tightly coupled windings on a shared magnetic core. Both primary and secondary currents are purely ac with zero average value, and energy transfer occurs instantaneously via magnetic coupling. In contrast, this coupled inductor configuration allows for input and output currents with nonzero average values, comprising a dc component with ac ripple, as shown in Fig. 1(b). The presence of a magnetic core is essential to its energy transfer mechanism, as it enables energy storage during the switching intervals.

Fig. 1(c) shows a classical WPT system based on air-core coils, where both the Tx and Rx carry pure ac currents. WPT methods can generally be categorized into magnetic resonance (MR) and IPT. MR systems typically operate in resonant and support long-distance power transfer, whereas IPT systems are mostly nonresonant and designed for mid-range transfer.

Finally, Fig. 1(d) shows the employed IPT-based method. The input current contains a dc component with ac ripples, while the output current exhibits purely ac characteristics.

From a waveform perspective, the presented method does not exactly match any of the conventional categories above. However, it differs fundamentally from the coupled inductor method in that it does not incorporate and rely on a magnetic core. Despite lacking strict electrical isolation, the presented method shares key IPT characteristics such as contactless energy transfer, physical removability, and magnetic coupling via air-core coils. Therefore, the presented method is most appropriately classified as a variant of IPT.

Besides, a notable limitation of the presented topology is that the Tx coil in the employed topology must handle a large current ripple to deliver balancing energy, which may impose additional ripple stress on components and lead to increased conduction losses. Nevertheless, the overall system stability and the operation of the main circuit remain unaffected. The key contributions of this work are given as follows.

1) An IPT-based battery equalizer is developed by replacing the inductor in a bidirectional converter with a Tx coil. By multiplexing the ac and dc components in the Tx coil current, wireless battery balancing is enabled during both charging and discharging processes.
2) To enable the single receiver structure, a switch matrix is introduced in this work, which eliminates cross-coupling issues associated with multireceiver configurations and provides the potential for bypassing faulty cells.
3) In this work, an efficient adaptive equalization algorithm, incorporating a connection duration controller, is presented to ensure accurate balancing and to minimize overall power losses during the equalization process.

The rest of this article is arranged as follows. Section II introduces the configuration and fundamental operating principles of the enhanced IPT-based battery equalizer. Section III details the control strategy. Experimental validation using a scaled-down prototype is presented in Section IV. Section V provides additional comments and insights on the presented method, followed by a comparative evaluation with existing equalizers in Section VI. Finally, Section VII concludes this article.

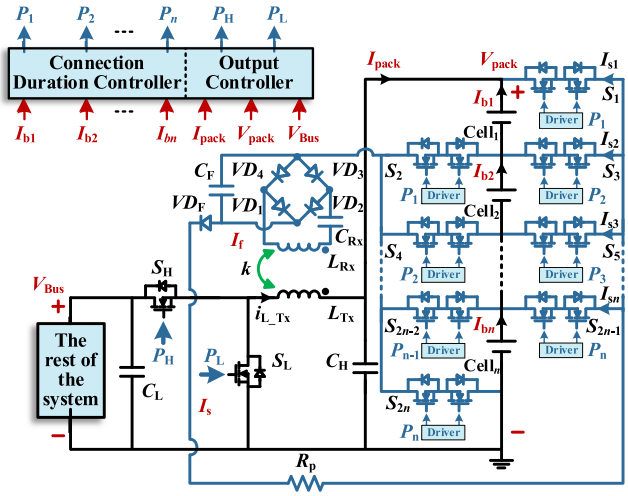

Fig. 2. Configuration of the IPT-based battery equalizer.

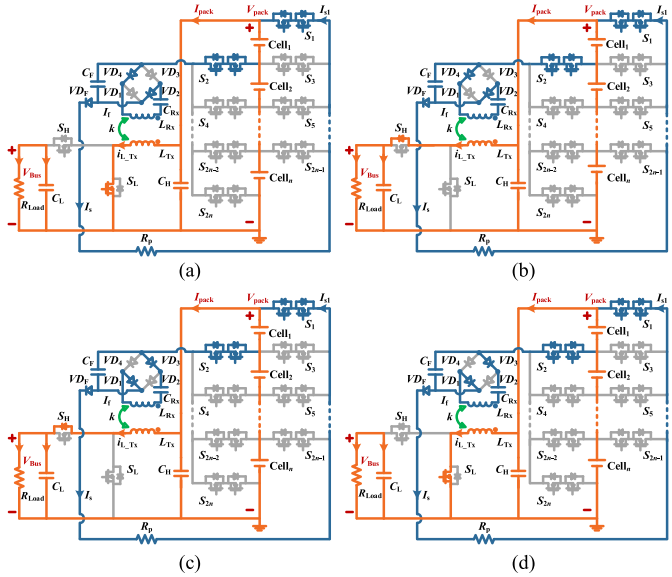

Fig. 3. Operating states during discharging mode. (a) State 1. (b) State 2. (c) State 3. (d) State 4.

II. Fundamental Analysis

This section elaborates on the configuration of the presented battery equalizer, comprising a bidirectional single-inductor dc–dc converter and a balancing circuit. Moreover, the direction of current is analyzed in both the charging and discharging processes, and both are divided into four operation stages in a switching period of the converter.

A. Structure of IPT-Based Equalizer

Fig. 2 shows the configuration of the presented IPT-based equalizer, which integrates a bidirectional single-inductor dc–dc converter (represented by the black line) with a balancing circuit (represented by the blue line).

The converter comprises two complementary MOSFETs, $S_{\rm H}$ and S_L, an inductor $L_{\rm Tx}$, and filter capacitors C_L and C_H. The right side of the converter is connected to a series of n battery cells, while the left side is connected to the rest of the system, including power sources for charging or loads for discharging.

Building on the introduced bi-directional single-inductor dc–dc converter, a balancing circuit is incorporated to enable the IPT process. In this circuit, the inductor $L_{\rm Tx}$ within the converter functions as a Tx coil for IPT. A single Rx coil $L_{\rm Rx}$, is coupled with $L_{\rm Tx}$ to wirelessly receive feedback energy via a coupling coefficient k. Diodes $\rm VD_1$–$\rm VD_4$ form a rectifier bridge following $L_{\rm Rx}$, which is connected to a filter capacitor C_F to prevent a rapid drop in Rx current. In addition, a diode $\rm VD_F$ is placed after the C_F to ensure unidirectional feedback current. The switch matrix, which is composed of dual n-channel common source MOSFETs as the sequential cell switches S_1–S_{2n}, directs wireless energy to the selected battery cell, with a detailed control strategy provided in Section III-B.

B. Discharging Mode

For the single Tx and single Rx system, the coupling efficiency k is typically high enough to ensure rectifier bridge conduction through proper design of the inductances, shape, and size of the coils. However, if k is extremely low, meaning the coils are barely coupled, the system naturally operates as a conventional converter, with the Rx side left open-circuited and no energy received.

When a load is connected to the left side of the presented bi-directional single-inductor dc–dc converter, the converter operates as a boost converter to discharge the battery pack. The load voltage is regulated by the duty cycle D_L of switch S_L. Using closed-loop control, the duty cycle D_L is adjusted to maintain a constant load voltage, denoted as $V_{\rm Bus}$.

For example, when the first battery cell $\rm Cell_1$ is selected, the converter's operation during discharging divides the switching period T_0 into four states based on the state and direction of the current $I_{\rm Tx}$ flowing through $L_{\rm Tx}$, as shown in Fig. 3. It is worth to highlight that during the entire discharging process, the current $I_{\rm Tx}$ consistently flows through $L_{\rm Tx}$ from right to left, which is defined as negative.

1) *State 1 (t_1–t_2):* As shown in Fig. 3(a), when the S_L is turned ON, current $I_{\rm Tx}$ flows through $L_{\rm Tx}$ with a raised absolute magnitude. A positive voltage is induced to the left of $L_{\rm Rx}$, thereby increasing the feedback current I_f flowing through from left to right, rendering $\rm VD_2$ and $\rm VD_4$ of the rectifier bridge conductive. By utilizing Kirchhoff's voltage law (KVL) in both the converter and balancing circuits, (1) can be derived. It is worth noting that while the diode drop is considered in the balancing loop (Rx side), it is neglected in the converter circuit (Tx side) due to the significantly higher voltage level of the converter

$$\begin{cases} V_{\rm Tx\_}D1 = -\frac{M}{L_{\rm Rx}} V_{\rm Rx\_}D1 - V_{\rm pack} \\ V_{\rm Rx\_}D1 = -\frac{M}{L_{\rm Tx}} V_{\rm Tx\_}D1 - V_{\rm drop} - V_F \end{cases} \tag{1}$$

where $V_{\rm Tx\_}D1$ and $V_{\rm Rx\_}D1$ denote the voltages across $L_{\rm Tx}$ and $L_{\rm Rx}$ in *State 1*, respectively. $V_{\rm pack}$ represents the voltage of the battery pack. In addition, V_F represents the terminal voltage of filter capacitor C_F, and $V_{\rm drop}$ denotes the total voltage drop across the IPT loop, including the rectifier. In this section, the

reference direction for the voltages V_{Tx} and V_{Rx} is defined as left positive and right negative.

According to (1), $V_{\mathrm{Tx\_D1}}$ and $V_{\mathrm{Rx\_D1}}$ in *State 1* during discharging mode can be solved as

$$\begin{cases} V_{\mathrm{Tx\_D1}} = -\frac{L_{\mathrm{Tx}}(L_{\mathrm{Rx}}V_{\mathrm{pack}} - M(V_F+V_{\mathrm{drop}}))}{L_{\mathrm{Tx}}L_{\mathrm{Rx}}-M^2} \\ V_{\mathrm{Rx\_D1}} = \frac{L_{\mathrm{Rx}}(MV_{\mathrm{pack}} - L_{\mathrm{Tx}}(V_F+V_{\mathrm{drop}}))}{L_{\mathrm{Tx}}L_{\mathrm{Rx}}-M^2} \end{cases}. \tag{2}$$

2) *State 2 (t_2–t_3):* As shown in Fig. 3(b), when the S_L is deactivating, the battery pack charges the load with a reduced absolute current I_{Tx}, maintaining the same direction as in *State 1*. A positive voltage is generated on the right side of L_{Rx}. However, due to the presence of L_{Rx}, the current flowing through L_{Rx} cannot be reversed immediately. The following KVL equation can be obtained as:

$$\begin{cases} V_{\mathrm{Tx\_D2}} = -\frac{M}{L_{\mathrm{Rx}}}V_{\mathrm{Rx\_D2}} + V_{\mathrm{Bus}} - V_{\mathrm{pack}} \\ V_{\mathrm{Rx\_D2}} = -\frac{M}{L_{\mathrm{Tx}}}V_{\mathrm{Tx\_D2}} - V_{\mathrm{drop}} - V_{\mathrm{F}} \end{cases}. \tag{3}$$

Therefore, $V_{\mathrm{Tx\_D2}}$ and $V_{\mathrm{Rx\_D2}}$ in *State 2* can be described as

$$\begin{cases} V_{\mathrm{Tx\_D2}} = \frac{L_{\mathrm{Tx}}(L_{\mathrm{Rx}}(V_{\mathrm{Bus}}-V_{\mathrm{pack}}) + M(V_F+V_{\mathrm{drop}}))}{L_{\mathrm{Tx}}L_{\mathrm{Rx}}-M^2} \\ V_{\mathrm{Rx\_D2}} = -\frac{L_{\mathrm{Rx}}(M(V_{\mathrm{Bus}}-V_{\mathrm{pack}}) + L_{\mathrm{Tx}}(V_F+V_{\mathrm{drop}}))}{L_{\mathrm{Tx}}L_{\mathrm{Rx}}-M^2} \end{cases}. \tag{4}$$

From (4), it is evident that the $V_{\mathrm{Rx\_D2}}$ assumes a negative value, causing the feedback current I_f to diminish, flowing from left to right. As I_f drops to zero, *State 2* ends.

3) *State 3 (t_3–t_4):* The switch S_L remains in the turned-OFF state as depicted in Fig. 3(c), indicating that the direction of the induced voltage across L_{Rx} remains the same as in *State 2*. However, after the current reset following *State 2*, the current flowing through L_{Tx} reverses its direction (from right to left), resulting in the conduction of VD_1 and VD_3 in the rectifier. The KVL equation can be given as

$$\begin{cases} V_{\mathrm{Tx\_D3}} = -\frac{M}{L_{\mathrm{Rx}}}V_{\mathrm{Rx\_D3}} + V_{\mathrm{Bus}} - V_{\mathrm{pack}} \\ V_{\mathrm{Rx\_D3}} = -\frac{M}{L_{\mathrm{Tx}}}V_{\mathrm{Rx\_D3}} + V_{\mathrm{drop}} + V_{\mathrm{F}} \end{cases}. \tag{5}$$

Through the resolution of (5), $V_{\mathrm{Tx\_D3}}$ and $V_{\mathrm{Rx\_D3}}$ in *State 3* can be denoted as

$$\begin{cases} V_{\mathrm{Tx\_D3}} = \frac{L_{\mathrm{Tx}}(L_{\mathrm{Rx}}(V_{\mathrm{Bus}}-V_{\mathrm{pack}}) - M(V_F+V_{\mathrm{drop}}))}{L_{\mathrm{Tx}}L_{\mathrm{Rx}}-M^2} \\ V_{\mathrm{Rx\_D3}} = -\frac{L_{\mathrm{Rx}}(M(V_{\mathrm{Bus}}-V_{\mathrm{pack}}) - L_{\mathrm{Tx}}(V_F+V_{\mathrm{drop}}))}{L_{\mathrm{Tx}}L_{\mathrm{Rx}}-M^2} \end{cases}. \tag{6}$$

4) *State 4 (t_4–t_5):* As shown in Fig. 3(d), upon activating the S_L, L_{Tx} is charged by the battery pack with an increased current. The induced voltage on the Rx side is positive left, while the current flowing through L_{Rx} maintains its direction as in *State 3*. This process can be characterized as

$$\begin{cases} V_{\mathrm{Tx\_D4}} = -\frac{M}{L_{\mathrm{Rx}}}V_{\mathrm{Rx\_D4}} - V_{\mathrm{pack}} \\ V_{\mathrm{Rx\_D4}} = -\frac{M}{L_{\mathrm{Tx}}}V_{\mathrm{Tx\_D4}} + V_{\mathrm{drop}} + V_F \end{cases}. \tag{7}$$

By deriving solutions from (7), $V_{\mathrm{Tx\_D4}}$ and $V_{\mathrm{Rx\_D4}}$ in *State 4* can be expressed as

$$\begin{cases} V_{\mathrm{Tx\_D4}} = -\frac{L_{\mathrm{Tx}}(L_{\mathrm{Rx}}V_{\mathrm{pack}} + M(V_F+V_{\mathrm{drop}}))}{L_{\mathrm{Tx}}L_{\mathrm{Rx}}-M^2} \\ V_{\mathrm{Rx\_D4}} = \frac{L_{\mathrm{Rx}}(MV_{\mathrm{pack}} + L_{\mathrm{Tx}}(V_F+V_{\mathrm{drop}}))}{L_{\mathrm{Tx}}L_{\mathrm{Rx}}-M^2} \end{cases}. \tag{8}$$

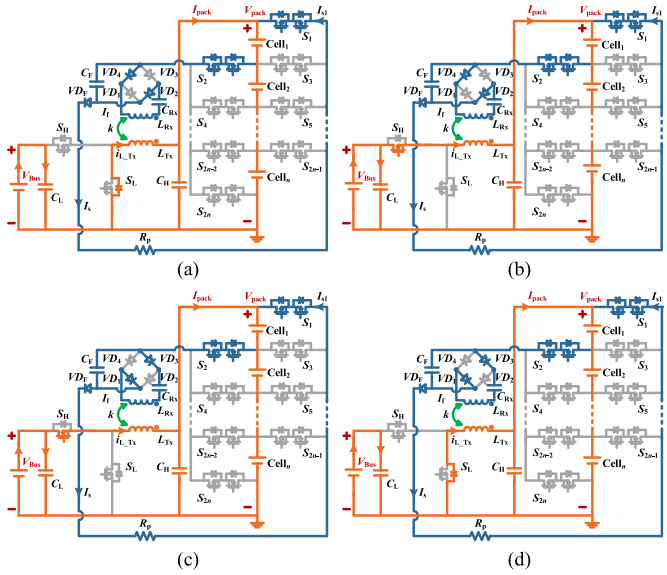

Fig. 4. Operating states during charging mode. (a) State 1. (b) State 2. (c) State 3. (d) State 4.

As shown in (8), it is apparent that the $V_{\mathrm{Rx\_D4}}$ returns to a positive value, prompting the resetting of the feedback current I_f, which flows from right to left. Once I_f reaches zero, *State 4* ends and *State 1* is restarted, marking the initiation of a new converter switching period T_0.

C. Charging Mode

When a high-voltage power source is connected to the input of the converter on the left side, the converter operates in charging mode, functioning as a buck converter. Similarly, the voltage of a high-power dc source is represented as V_{Bus}. The charging voltage and current are determined by the duty cycle D_H of switch S_H. The constant current constant voltage charging strategy is employed for battery protection.

In the charging mode, the system manifests four operating states within a converter switching period T_0, as shown in Fig. 4 with a relatively high coupling efficiency k. Although the current I_{Tx} through inductor L_{Tx} flows in opposite directions during charging compared to discharging, the current loop structure remains similar in both modes. Consequently, the KVL equations derived for the discharging process are also applicable during charging, resulting in analogous expressions for V_{Tx} and V_{Rx}, as derived from (2), (4), (6), and (8).

D. Operating Principle of the Balancing Switch Matrix

To accommodate a single Rx coil configuration, a switch matrix is employed to sequentially connect the Rx circuit to each individual battery cell. This subsection illustrates how the switch matrix coordinates with the Rx coil to enable cell balancing under different operating states.

As an illustrative example, Fig. 5 shows the current flow paths during *State 1* of the discharging mode in a four-cell pack. Although different combinations of switches are activated depending on the selected cell, the resulting current loops follow a

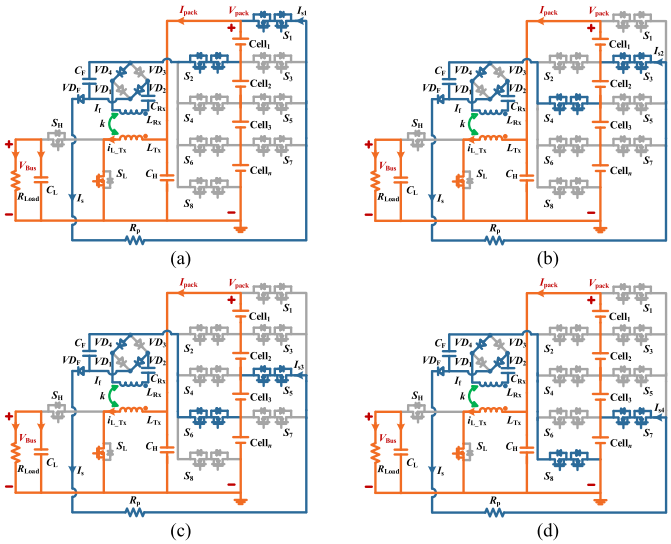

Fig. 5. Current flow paths in *State 1* during discharging. (a) Cell_1 is selected. (b) Cell_2 is selected. (c) Cell_3 is selected. (d) Cell_4 is selected.

TABLE I
TURNED-ON SWITCHES FOR EACH BALANCING STATE AND CELL CONNECTION IN A FOUR-CELL PACK

	Cell_1	Cell_2	Cell_3	Cell_4
State 1	S_L, S_1, and S_2	S_L, S_3, and S_4	S_L, S_5, and S_6	S_L, S_7, and S_8
State 2	S_H, S_1, and S_2	S_H, S_3, and S_4	S_H, S_5, and S_6	S_H, S_7, and S_8
State 3	S_H, S_1, and S_2	S_H, S_3, and S_4	S_H, S_5, and S_6	S_H, S_7, and S_8
State 4	S_L, S_1, and S_2	S_L, S_3, and S_4	S_L, S_5, and S_6	S_L, S_7, and S_8

consistent structural pattern, ensuring the balancing mechanism functions uniformly across all cells.

To further clarify the operating principle of the switch matrix, the turned-ON switch combinations for each state and selected cell are summarized in Table I. This switching strategy ensures that each cell can be individually connected for balancing without interference or cross-coupling.

It is worth noting that although the switching structure remains similar across different cell selections, the actual current values vary depending on the terminal voltage of the connected cell. Detailed analysis of the feedback current, shunt current, and control strategy is provided in Section III.

III. DISCUSSION OF THE BALANCING STRATEGY

In this section, the relationship between the feedback current and the voltage of the filter capacitors is analyzed and discussed. Based on this analysis, an efficient adaptive equalization algorithm is introduced, which allocates the connection duration for each battery cell.

A. Analysis of the Feedback Current

Both the discharging and charging modes demonstrate that V_{TX} and V_{RX} exhibit analogous behavior within the same operational state in each mode. As a result, the principal waveforms of the PWM signals for S_L and S_H, the feedback current I_f, Tx

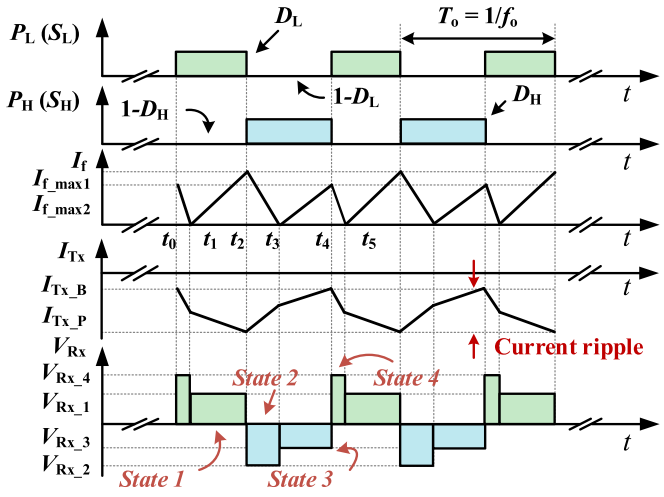

Fig. 6. Key waveform of PWM signals, feedback current I_f, current I_{Tx} of transmitter coil, and voltage V_{RX} of receiver coil in discharging mode.

coil's current I_{Tx} (defined as negative), and the voltage V_{RX} of the Rx coil during the discharging process are demonstrated as an example in Fig. 6.

From Fig. 6, with t_0 defined as the initial time and set to zero, the relationship among t_2, t_4, D_{H}, D_{L}, and T_0 can be given as

$$t_2 = D_L\, T_o = \ (1 - D_H)\, T_0 \tag{9}$$

$$t_4 = T_0 \tag{10}$$

where T_0 is the switching period of the converter. Assuming the system reaches a steady state, (11) and (12) are derived based on the inductor volt-second balance principle

$$(t_2 - t_1) \times V_{\text{Rx\_}D1} + (t_3 - t_2) \times \ V_{\text{Rx\_}D2} = \ 0 \tag{11}$$

$$(t_4 - t_3) \times V_{\text{Rx\_}D3} + (t_5 - t_4) \times \ V_{\text{Rx\_}D4} = \ 0. \tag{12}$$

In steady-state conditions, the duration from t_4 to t_5 is equal to the interval from t_0 to t_1. When the converter circuit operates in continuous current mode, the time intervals from t_0 to t_4 satisfy

$$0 \ = V_{\text{Tx\_}D1}\ (t_2 - t_1) + V_{\text{Tx\_}D2}\,(t_3 - t_2)\ + V_{\text{Tx\_}D3}\,(t_4 - t_3) + V_{\text{Tx\_}D4}\,(t_5 - t_4)\,. \tag{13}$$

Combining (11)–(13), t_1, t_3, and V_{Bus} can be resolved as

$$t_1 = T_0\ \frac{D_L M V_{\text{pack}} - L_{\text{Tx}} D_H\,(V_F + V_{\text{drop}})}{2MV_{\text{pack}}} \tag{14}$$

$$t_3 = T_0\ \frac{(1 + D_L)\,MV_{\text{pack}} - L_{\text{Tx}} D_H\,(V_F + V_{\text{drop}})}{2MV_{\text{pack}}} \tag{15}$$

$$V_{\text{Bus}} = \frac{V_{\text{pack}}}{D_H}\ = \frac{V_{\text{pack}}}{1 - D_L}\,. \tag{16}$$

As shown in (16), although energy is transmitted back to the battery pack through IPT, the output characteristics of the bi-directional dc–dc converter remain unaffected, whether operating in buck or boost mode.

According to (14) and (15), the current ripple ΔI_{Tx} of the Tx coil (converter's inductor) in the presented equalizer can be

TABLE II
PARAMETERS USED TO CALCULATE AVERAGE FEEDBACK CURRENT IN FIG. 7

Symbol	Value	Symbol	Value
f_0	200 kHz	L_{Tx}	12.7 μH
V_{Bus}	38 V	L_{Rx}	10 μH
k	0.82	D_{L}	0.25–0.75
V_{drop}	0.7 V	V_{F}	2.75–4.2 V

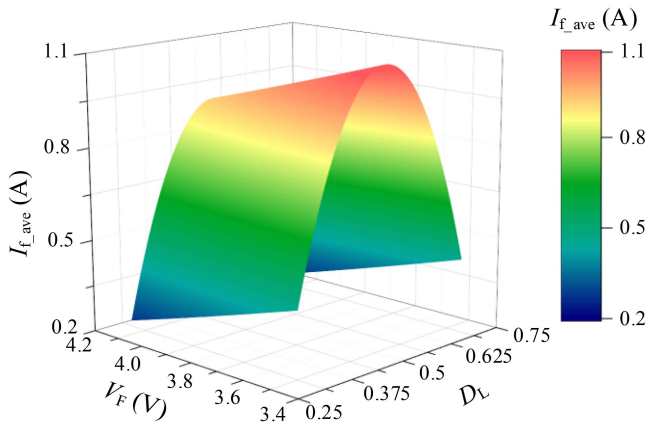

Fig. 7. Three-dimensional plot of I_{f_ave} as a function of filter capacitor voltage V_F and duty cycle D_L based on the parameters listed in Table II.

expressed as

$$\Delta I_{\mathrm{Tx}} = \frac{V_{\mathrm{Tx\_}D2}}{L_{\mathrm{Tx}}}\ (t_3 - t_2) + \frac{V_{\mathrm{Tx\_}D3}}{L_{\mathrm{Tx}}}\,(t_4 - t_3) = \frac{T_0\left(L_{\mathrm{Rx}}V_{\mathrm{pack}}\,(V_{\mathrm{Bus}} - V_{\mathrm{pack}}) - L_{\mathrm{Tx}}(V_F + V_{\mathrm{drop}})^2\right)}{V_{\mathrm{Bus}}\,(L_{\mathrm{Tx}}L_{\mathrm{Rx}} - M^2)}. \tag{17}$$

Furthermore, $I_{f\_\max1}$ and $I_{f\_\max2}$ can be derived as

$$I_{f\_\max1} = V_{\mathrm{Rx\_}D1}\ (t_2 - t_1) \tag{18}$$

$$I_{f\_\max2} = V_{\mathrm{Rx\_}D3}\ (t_4 - t_3)\,. \tag{19}$$

Ultimately, the average feedback current I_{f_ave} could be calculated as

$$I_{f\_ave} = \frac{I_{f\_\max1}\,(t_3 - t_1) + I_{f\_\max2}\,(t_1 + t_4 - t_3)}{2T_0}\,. \tag{20}$$

By substituting (14) through (19) into (20), (21) shown at the bottom of this page, is derived, where f_0 represents the switching frequency of the converter. It is evident that the average feedback current I_{f_ave} is inversely proportional to f_0.

To further investigate the relationship between I_{f_ave}, D_L, and V_F, the values of I_{f_ave} corresponding to different terminal voltages V_F of the filter capacitor C_F and D_L are calculated using the parameters listed in Table II, as shown in Fig. 7.

As illustrated in Fig. 7, a lower V_F leads to a higher average feedback current I_{f_ave}, indicating that more energy is transferred back to the lower-voltage battery cell over the same period. Furthermore, as the duty cycle D_L approaches 0.5, the average feedback current increases, peaking at 1.124 A when V_F is 3.4 V and D_L is 0.5. In addition, the dynamic equation of V_F can be represented as

$$C_F\,\frac{dV_F}{dt} = I_{f\_ave} - I_{si} = I_{f\_ave} - \frac{V_F - V_{\mathrm{b}i} - V_d}{R_p} \tag{22}$$

where $I_{\mathrm{s}i}$ and $V_{\mathrm{b}i}$ represent the shunt current and terminal voltage of the ith battery cell, respectively, V_d is the forward voltage drop of diode VD_F, and R_P is the parasitic resistance.

It is observed that as $V_{\mathrm{b}i}$ increases, V_F increases accordingly, leading to a reduced average feedback current I_{f_ave}. This reduction in I_{f_ave} results in a lower shunt current $I_{\mathrm{s}i}$ in the steady state. Thus, higher values of $V_{\mathrm{b}i}$ are associated with decreased values of both I_{f_ave} and $I_{\mathrm{s}i}$ in the steady state.

B. Introduction of the Adaptive Equalization Algorithm

Although the negative relationship is provided in Section III-A, the equalization speed appears slow if it depends on a constant connection duration for all cells. To address this, an efficient adaptive equalization algorithm is introduced for a battery pack with n cells, as shown in Fig. 8(a).

At the beginning of each cycle, the SOC values for each cell are updated. If the difference between the maximum SOC ($\mathrm{SOC}_{\max}$) and the minimum SOC ($\mathrm{SOC}_{\min}$) is below a specified threshold δ, the system is considered balanced. Consequently, all cell switches are deactivated, halting the IPT process to improve overall efficiency.

Conversely, if the difference between $\mathrm{SOC}_{\max}$ and $\mathrm{SOC}_{\min}$ exceeds the threshold δ, the system is seen as being in an imbalanced condition. In this case, the connection duration controller adjusts the connection times for each cell based on its SOC value, as illustrated in Fig. 8(b). Each cell is sequentially connected to the Rx for an adaptive duration within a constant total cycle time T_f. Finally, the discharging or charging current of each cell is measured to update the SOC values for the subsequent cycle.

To reach effective balancing, the connection duration controller calculates the average SOC value, which is given as

$$\mathrm{SOC}_{\mathrm{ave}} = \frac{\sum_{i=1}^{n}\mathrm{SOC}_i}{n} \tag{23}$$

where SOC_i represents the SOC of the ith cell. The deviations between SOC_i and $\mathrm{SOC}_{\mathrm{ave}}$ are processed by the duration compensator, which is represented by the continuous-time function $G_{\mathrm{duration}}(s)$ or the discrete-time transfer function $G_{\mathrm{duration}}(z)$. In this article, $G_{\mathrm{duration}}(z)$ is utilized and defined as

$$G_{\mathrm{duration}}\,(z) = K_{P\_\mathrm{duration}} + \frac{K_{I\_\mathrm{duration}}}{z - 1} \tag{24}$$

$$I_{f\_ave} = \frac{(D_{\mathrm{H}}MV_{\mathrm{Bus}} - L_{\mathrm{Tx}}\,(V_F + 2V_{\mathrm{drop}})) \times (D_H D_L MV_{\mathrm{Bus}} - L_{\mathrm{Tx}}D_H\,(V_F + 2V_{\mathrm{drop}}))}{4f_0 M D_H V_{\mathrm{Bus}}\,(L_{\mathrm{Tx}}L_{\mathrm{Rx}} - M^2)} \tag{21}$$

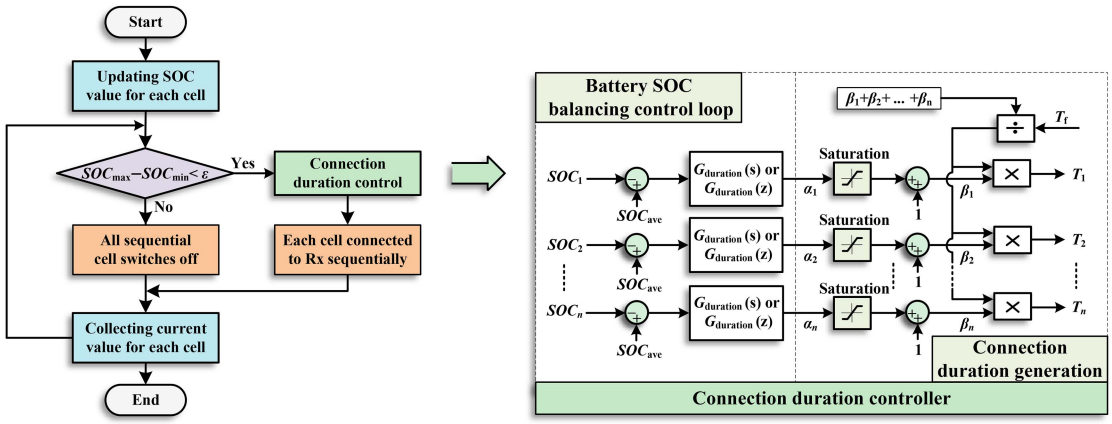

Fig. 8. SOC equalization control strategy. (a) Introduced efficient adaptive equalization algorithm. (b) Connection duration controller.

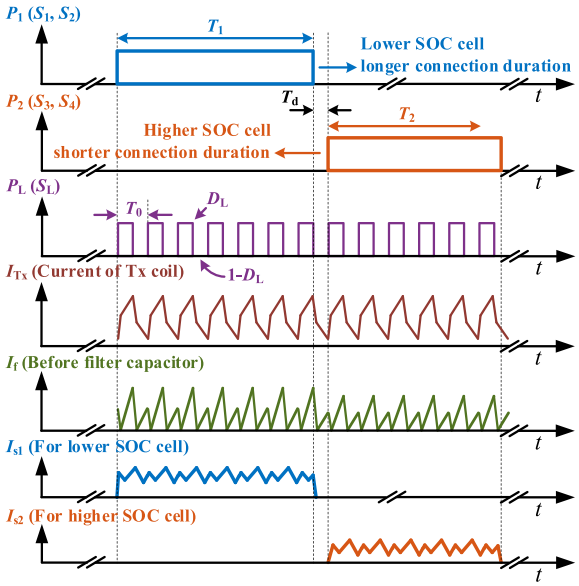

Fig. 9. Illustration of connection durations regulated by the controller and the key waveforms of the presented equalizer.

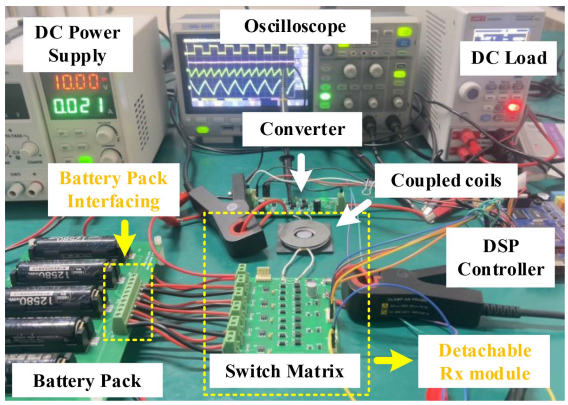

Fig. 10. Experimental prototype of the equalizer for five battery cells.

where $K_{P\_duration}$ and $K_{I\_duration}$ are the proportional and integral gains, respectively. The output α_i of the ith duration compensator is processed through a saturation module, and the duration multiplier β_i for the ith battery cell can be given as

$$\beta_i = \begin{cases} 0, & \alpha_i < -1 \\ \alpha_i + 1, & -1 \le \alpha_i \le 1. \\ 2, & \alpha_i > 1 \end{cases} \tag{25}$$

Based on the computed duration multipliers β_1 to β_n, the connection duration T_i for the ith battery cell can be given as

$$T_i = \frac{\beta_i}{\sum_{i=1}^{n} \beta_i} \times T_f \tag{26}$$

where T_f denotes the predefined constant total cycle time of the switch matrix.

An expanded view of Figs. 6 and 9 depicts the switching signals of cell switches S_1–S_4, the low-side switch drive signal S_L, the inductor current I_{Tx}, the feedback current I_f, and the shunt currents I_{s1} and I_{s2} during discharging as an instance.

The controller assigns longer connection intervals to cells with lower SOC and shorter intervals to those with higher SOC. To realize this, when balancing the ith cell, the switches $S_{2i\text{-}1}$ and S_{2i} in the switch matrix are turned on to connect this cell to the balancing circuit. Moreover, as derived in (20), a cell with higher SOC exhibits an elevated terminal voltage, which in turn reduces its feedback and shunt currents. By leveraging the intrinsic behavior of the equalizer topology together with the connection duration controller, the presented system achieves effective and precise balancing performance that significantly outperforms passive VEs.

IV. Experimental Results

To validate the presented IPT-based equalizer and the equalization control strategy, a down-scaled proof-of-concept prototype with five series-connected cells was developed in the laboratory, as depicted in Fig. 10.

The prototype utilizes a bidirectional, single-inductor dc–dc converter that handles both charging and discharging of the battery pack, employing IRLR120NTRPBF n-channel MOSFETs paired with SS56 Schottky diodes and all driven by the

TABLE III
SPECIFIC PARAMETERS OF THE BUILT EXPERIMENTAL PROTOTYPE

Symbol	Description	Value
f_0	Converter switching frequency	200 kHz
T_f	Total cycle time for switch matrix	0.1 s
V_{bi}	Voltage of the ith battery cell	2.75 – 4.2 V
V_{pack}	Voltage of the battery pack	13.75–21 V
V_{Bus}	Rated bus voltage of the dc–dc converter	38 V
V_{drop}	Total voltage drop across the IPT loop	0.7 V
Q_{Cell}	Capacity of the utilized battery cell	3400 mAh
I_C	Reference battery pack charging current	1.7 A
R_{Load}	Nominal resistive load during discharging	40 Ω
C_F	Capacitance of the filter capacitor	22 μF
L_{Tx}	Inductance of Tx coil	12.7 μH
L_{Rx}	Inductance of the Rx coil	10 μH
k	Coupling coefficients between L_{Tx} and L_{Rx}	0.82

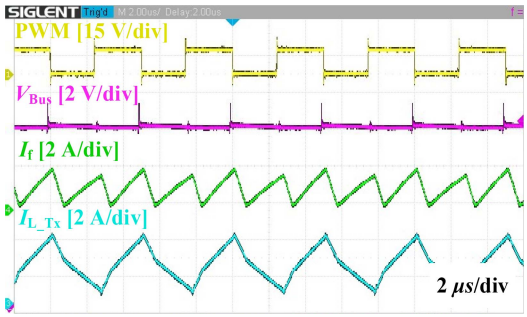

Fig. 11. Waveforms of the PWM signal for S_H, output voltage V_{Bus}, current I_{Tx}, and feedback current I_f during discharging.

LM5109BMAX/NOPB gate driver. The QS5K2 dual n-channel common-source MOSFETs form the switch matrix and are also controlled by the same gate driver. The battery pack, consisting of five 18650-type lithium-ion cells in series (3.7 V nominal, 3400 mAh), is connected to the converter's right side. Depending on the operating mode, the converter's left side is connected either to a programmable dc electronic load (for discharge tests) or to a high-voltage dc source (for charging). Detailed specifications of the IPT-based equalizer are provided in Table III.

A. Discharging Experiment Results

During a rated discharging process, a dc electronic load with a resistance of 40 Ω is connected to the left side of the presented bidirectional single-inductor dc–dc converter.

Fig. 11 illustrates the waveforms of the PWM signal for the high-side switch S_H, the output voltage V_{Bus}, the current I_{Tx} through the Tx coil L_{Tx}, and the feedback current I_f. The slope of I_{Tx} varies according to the operating states shown in Fig. 6, while the output voltage V_{Bus} follows the reference value and remains unaffected by the IPT process, which aligns with the theoretical analysis presented in Section III-A.

The balancing experimental results are presented in Fig. 12, where the initial SOC values of the battery cells are 0.96, 0.935, 0.91, 0.885, and 0.86, respectively. To emulate realistic load

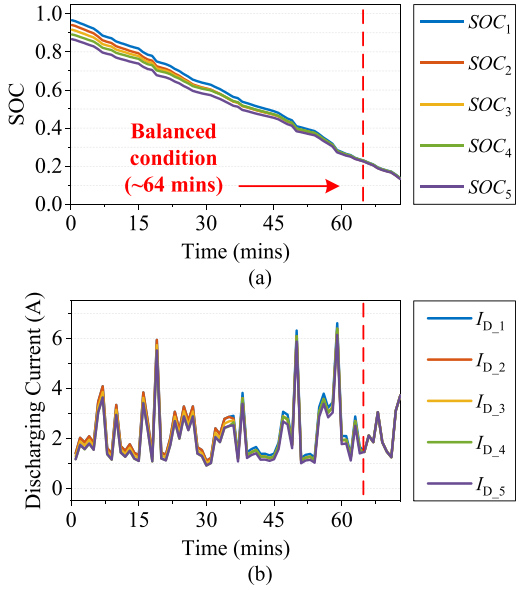

Fig. 12. Experimental balancing result of each battery cell in real load current discharging. (a) SOC values. (b) Discharging currents.

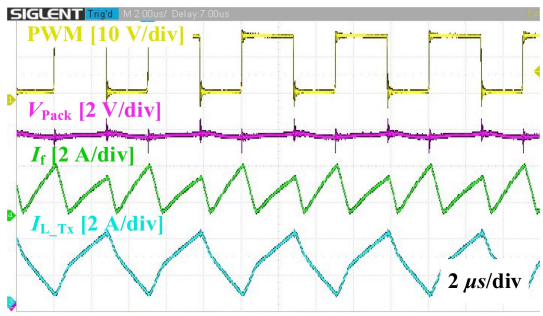

Fig. 13. Waveforms of the PWM signal for S_H, output voltage V_{Bus}, current I_{Tx}, and feedback current I_f during charging.

dynamics, the discharging current follows a scaled-down profile derived from an electric aerial lift vehicle battery pack [31], [32], and is applied using a programmable dc electronic load. This current profile includes high-frequency and abrupt fluctuations, effectively reflecting real-world conditions.

The SOC values and discharging currents of each cell, as shown in Fig. 12(a) and (b), demonstrate that the equalizer effectively balances the SOC of the battery pack despite the dynamic variations in load current. The maximum SOC discrepancy decreases from 10% to 0.5% within 64 min, highlighting the equalizer's capability to achieve precise and robust balancing even under realistic discharge scenarios.

B. Charging Experimental Results

When a high-voltage power source is connected to the left side, the bidirectional single-inductor dc–dc converter operates in buck mode to charge the battery pack at a 0.5 C rate, i.e., 1.7 A. The waveforms of the PWM signal for the low-side switch S_L, the charging voltage V_{Pack}, the current I_{Tx} through the Tx coil L_{Tx}, and the feedback current I_f are shown in Fig. 13. These

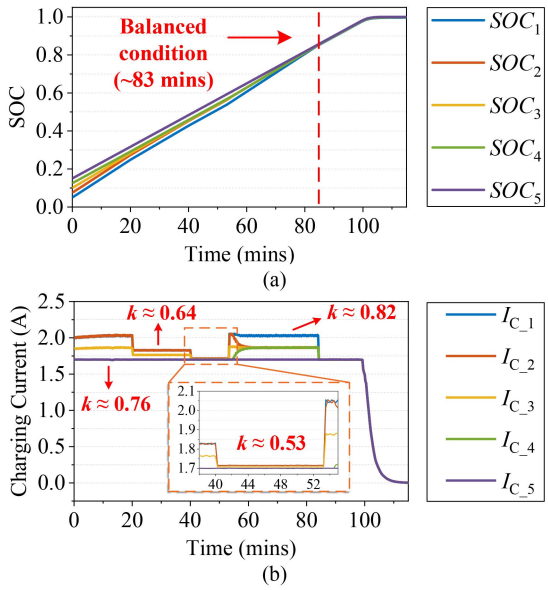

Fig. 14. Experimental balancing result of each battery cell under varying coupling conditions during charging. (a) SOC values. (b) Charging currents.

waveforms are consistent with the expected shapes presented in Fig. 9, regardless of whether the system is in charging or discharging mode.

Furthermore, Fig. 14 illustrates the experimental results of the IPT-based equalizer during the charging process, where the initial SOC values of the battery cells are 0.05, 0.075, 0.1, 0.125, and 0.15, respectively. To evaluate the system's performance under varying magnetic coupling conditions, the experiment introduces three representative levels of coil misalignment: slight ($k = 0.76$), moderate ($k = 0.64$), and severe ($k = 0.53$), in addition to the aligned condition ($k = 0.82$) considered as the rated case.

As shown in Fig. 14, the shunt current decreases with weakening coupling and increases again once realignment is restored. Despite these variations, the equalizer effectively reduces the maximum SOC difference from 10% to 0.5% within 83 min, demonstrating strong robustness against magnetic coupling changes. While a higher coupling coefficient enhances the balancing speed, it may also lead to greater power loss. In this article, the aligned condition is designed as the rated operating scenario to illustrate a fast and effective balancing performance. In practice, the rated coupling coefficient can be further optimized to meet specific application requirements.

C. Efficiency Analysis

Although the operational characteristics of the integrated bidirectional single-inductor dc–dc converter remain unaffected by the IPT process, its efficiency is significantly lower compared to conventional converters. To assess the impact of IPT on overall efficiency over the entire charging or discharging process, average efficiencies are employed here. During the balancing interval from the beginning of operation (t_0) to the time when balancing is achieved (t_B), the average discharging efficiency of

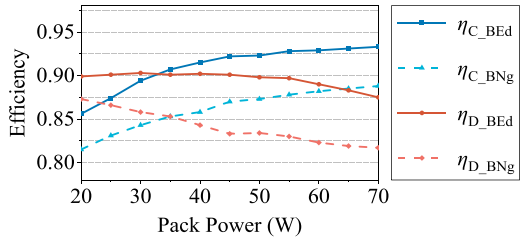

Fig. 15. Average efficiency of the introduced equalizer under varying pack power levels and operational modes.

the equalizer is expressed as

$$\eta_{\mathrm{D\_BNg}} = \frac{100\%}{t_{\mathrm{B}} - t_0} \int_{t_0}^{t_{\mathrm{B}}} \frac{V_{\mathrm{Bus}} I_{\mathrm{Bus}} + \sum_{i=1}^{n} I_{\mathrm{s}i} V_{\mathrm{b}i}}{V_{\mathrm{pack}} I_{\mathrm{pack}}} dt. \quad (27)$$

Similarly, the average charging efficiency during balancing is calculated as

$$\eta_{\mathrm{C\_BNg}} = \frac{100\%}{t_{\mathrm{B}} - t_0} \int_{t_0}^{t_{\mathrm{B}}} \frac{V_{\mathrm{pack}} I_{\mathrm{pack}} + \sum_{i=1}^{n} I_{\mathrm{s}i} V_{\mathrm{b}i}}{V_{\mathrm{Bus}} I_{\mathrm{Bus}}} dt \quad (28)$$

where I_{si} and V_{bi} represent the shunt current and terminal voltage of the ith battery cell.

It is worth noting that when the system transitions to the balanced state at t_B, the feedback power $\sum_{i=1}^{n} I_{si} V_{bi}$ drops to zero, eliminating the power loss associated with the IPT process. Hence, during the interval from t_B to the end of operation (t_E), the average efficiencies are simplified as

$$\eta_{\mathrm{D\_BEd}} = \frac{1}{t_E - t_B} \int_{t_B}^{t_E} \frac{V_{\mathrm{Bus}} I_{\mathrm{Bus}}}{V_{\mathrm{pack}} I_{\mathrm{pack}}} dt \times 100\% \quad (29)$$

$$\eta_{\mathrm{C\_BEd}} = \frac{1}{t_E - t_B} \int_{t_B}^{t_E} \frac{V_{\mathrm{pack}} I_{\mathrm{pack}}}{V_{\mathrm{Bus}} I_{\mathrm{Bus}}} dt \times 100\% \quad (30)$$

where $\eta_{\mathrm{D\_BEd}}$ and $\eta_{\mathrm{C\_BEd}}$ represent the average discharging and charging efficiencies after balancing.

Fig. 15 presents the efficiency of the IPT-based equalizer under various pack power levels and operational modes. The experimental results show improved efficiency in the balanced state, as the adaptive equalization algorithm halts the IPT process once the battery pack reaches the balanced state. During charging, the efficiency at 40 W increases from 85.8% (in the balancing state) to 91.5% (in the balanced state), representing a 5.7% absolute improvement. Similarly, for discharging, the efficiency increases from 84.3% to 90.2%, yielding a 5.9% absolute gain at the same power level.

In addition, the observed difference in efficiency is due to lower switch voltage stress in buck mode (charging), resulting in reduced switching losses and higher efficiency.

During the charging process at a 0.5 C rate (pack current of 1.7 A), the system operates with a bus power of 36.23 W under balanced state and 38.5 W under balancing state. The average feedback current I_{f_ave} is calculated as 1.05 A based on (21). According to the datasheets, the MOSFETs used have a conduction resistance of 185 mΩ, with rise and fall times of 35 and 22 ns, respectively. The dc resistances of the Tx and Rx coils are 0.46 and 0.42 Ω, with rectifier and diode voltage drops of 0.7 and 0.4 V, respectively.

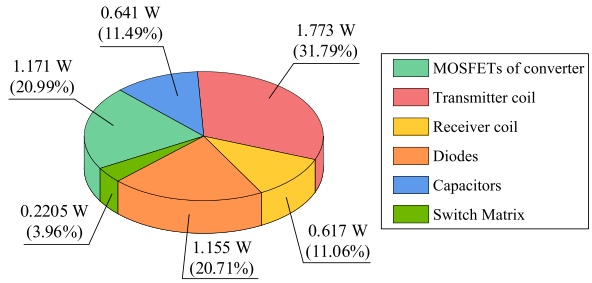

Fig. 16. Calculated power losses of the proposed system during 0.5 C charging operation.

TABLE IV
DIFFERENT CONTROL PARAMETERS FOR THE RESULTS OF FIG. 17

Figures	$K_{\text{P-soc}}$	$K_{\text{I-soc}}$	Balancing time
Fig. 17(a)	2.5	0.01	67 min
Fig. 17(b) (Employed)	5.5	0.02	62.5 min
Fig. 17(c)	11	0.06	62 min

Based on these parameters, the calculated power losses are: 1.171 W in converter MOSFETs, 1.155 W in the diodes, 0.221 W in capacitors, 1.773 W in the Tx coil, 0.617 W in the Rx coil, and 0.2205 W in the switch matrix. The calculated losses under the balancing state deviate by 4.6% from the measured values, and the deviation under the balanced state is 3.89%. Due to parasitic parameters and modeling simplifications, these errors are reasonable and acceptable. The summarized power losses of the presented equalizer are shown in Fig. 16.

V. ADDITIONAL COMMENTS

A. Parameter Tuning of Connection Duration Controller

As shown in Fig. 8(a), the adaptive equalization algorithm terminates the balancing process once the maximum SOC difference drops below the predefined threshold. To isolate and evaluate the dynamic response of the connection duration controller, the adaptive equalization algorithm is deactivated here, allowing investigation of equalization performance under different proportional-integral (PI) controller parameters.

Fig. 17 illustrates the shunt currents and SOC values of the battery cells during 0.5 C charging under three different sets of PI parameters, which are detailed in Table IV. The initial SOC values of Cell_1 to Cell_5 are set to 0.5, 0.75, 0.1, 0.125, and 0.15, respectively, with a maximum SOC error of 10%.

With smaller proportional and integral gains ($K_{\text{P-soc}} = 2.5$, $K_{\text{I-soc}} = 0.01$), as shown in Fig. 17(a), the controller exhibits a slower dynamic response, requiring approximately 67 min to achieve convergence of the shunt currents. Increasing the gains to $K_{\text{P-soc}} = 5.5$ and $K_{\text{I-soc}} = 0.02$, as illustrated in Fig. 17(b), the balancing speed is significantly improved, reducing the convergence time to 62.5 min while maintaining smooth and stable shunt current profiles. Further increasing the gains to $K_{\text{P-soc}} = 11$ and $K_{\text{I-soc}} = 0.06$, as depicted in Fig. 17(c), slightly reduces the balancing time to 62 min, at the expense of introducing noticeable oscillations in the charging current due to the more aggressive control action.

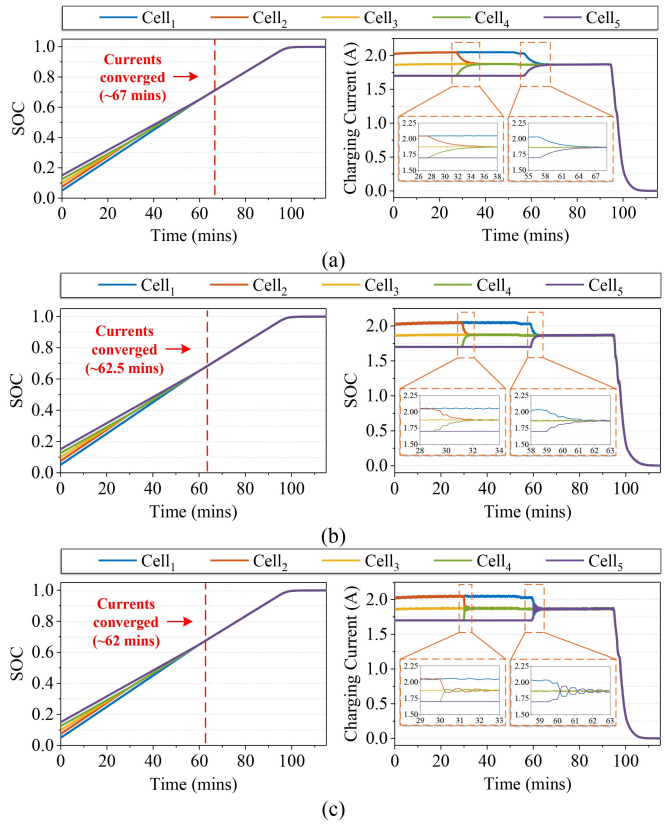

Fig. 17. Shunt current and SOC values for battery cells with different control parameters. (a) $K_{\text{P-soc}} = 2.5$ and $K_{\text{I-soc}} = 0.01$. (b) $K_{\text{P-soc}} = 5.5$ and $K_{\text{I-soc}} = 0.02$. (c) $K_{\text{P-soc}} = 11$ and $K_{\text{I-soc}} = 0.06$.

It is worth noting that increasing the PI gains beyond the values shown in Fig. 17(b) does not significantly reduce the balancing time, mainly due to the saturation module limiting the connection duration controller. In summary, tuning the connection duration controller involves a tradeoff between faster convergence and system stability. The parameters used in Fig. 17(b) strike an effective balance, enabling both rapid and stable SOC equalization.

B. Comparison of Different Balancing Strategies

Although a PI controller is utilized in the connection duration control scheme, it is necessary to compare it with other strategies to comprehensively evaluate the balancing performance under different equalization algorithms on the current experimental platform. As in Section V-A, the adaptive equalization algorithm is deactivated in this analysis to isolate the effects of the duration control strategies.

Three control strategies are implemented and tested on the same experimental platform: the introduced PI controller, a droop-inspired control, and a fixed-duration scheme, which represents a widely employed voltage-based balancing control [18], [19], [20], [21], [22], [23], [24]. The voltage-based approach relies on the negative relationship between the balancing current (shunt current) and the cell voltage, given as (21).

To clearly highlight performance differences, the controller parameters are scaled down compared to those listed in Table IV.

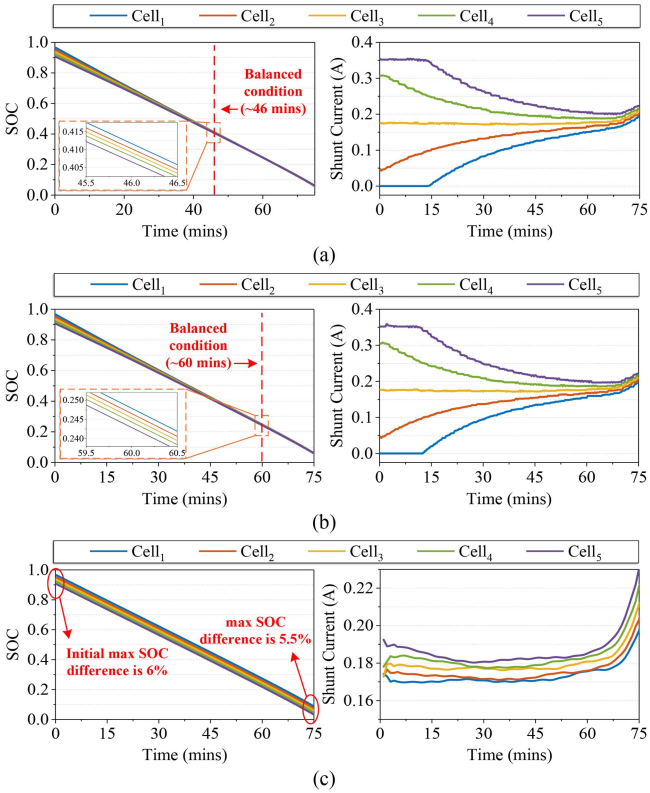

Fig. 18. Comparison of balancing performance under different connection duration control methods. (a) Employed PI controller ($K_{\text{P-soc}} = 1$, $K_{\text{I-soc}} = 0.01$). (b) Droop-inspired control. (c) Fixed-duration strategy.

Fig. 18 presents the SOC values and shunt currents of each cell under a constant load resistance of 40 Ω and a target bus voltage of 38 V. In which the initial SOC values of the five cells are 0.965, 0.95, 0.935, 0.92, and 0.905, respectively, resulting in a maximum initial SOC deviation of 6%. Moreover, the balanced state is defined as a maximum SOC discrepancy of 0.5%.

As shown in Fig. 18(a), the employed PI-controlled method ($K_{\text{P-soc}} = 1$, $K_{\text{I-soc}} = 0.01$) demonstrates the fastest convergence, achieving the balanced state within 46 min, while ensuring smooth current transitions and maintaining high balancing accuracy. The droop-inspired control ($m = 1$), with its linear response to SOC deviation and lack of integral compensation, achieves balancing in 60 min but converges slowly as the SOC differences further reduce. Meanwhile, the fixed-duration scheme exhibits markedly slower performance, reducing the initial SOC spread from 6% to only about 5.5% after 75 min. This limited effectiveness results from the small voltage differences among cells with close SOC values and the flat voltage plateaus in the lithium-ion battery open-circuit voltage curve [33], [34], both of which weaken the sensitivity and effectiveness of voltage-based balancing.

C. Tradeoff Between Balancing and Efficiency

Replacing the conventional inductor in a bidirectional converter with a Tx coil enables wireless transfer of the coil's current ripple energy. Since the balancing rate scales with ripple amplitude, balancing capability can be boosted by either reducing the effective inductance of the Tx coil (hardware modification) or lowering the switching frequency of the introduced converter (software adjustment). Generally, the latter is preferred due to its greater implementation flexibility.

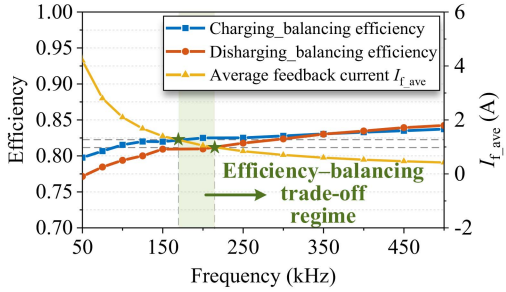

Fig. 19. Charging efficiency, discharging efficiency, and average feedback current $I_{\text{f\_ave}}$ as functions of the converter's switching frequency.

However, indiscriminately reducing the switching frequency of the employed converter is not advisable. As the frequency decreases, the current ripple grows, which can increase conduction losses and degrade overall converter performance. To identify the optimal operating range, the charging efficiency and discharging efficiency are measured and illustrated in Fig. 19, along with the average feedback current $I_{\text{f\_ave}}$ calculated by (21).

As shown in Fig. 19, the frequency band between the intersections of the $I_{\text{f\_ave}}$ curve with the efficiency curves is defined as the efficiency-balancing tradeoff region, which spans approximately 170–210 kHz. Operating below this range prioritizes faster balancing but reduces efficiency, while operating above it improves efficiency at the cost of slower balancing. In this work, the switching frequency of 200 kHz is selected as a suitable compromise.

D. Potential for Bypass of Faulty Cells

In a typical series-connected battery pack, the failure of a single cell requires that cell to be electrically disconnected to prevent damage and ensure safety. However, once a faulty cell is cut off, the resulting open-circuit condition can interrupt the current path and disable the entire string, unless an alternative path is provided. In the original equalizer design (as shown in Fig. 2), an n-cell pack required only n drive signals by pairing adjacent MOSFET modules to share each gate drive. Specifically, switches S_{2i-1} and S_{2i} in the switch matrix are turned ON simultaneously to connect Cell_i to the Rx circuit for balancing, which effectively reduces the overall cost and volume of the system. However, this shared-signal design is incompatible with the fault bypassing control strategy for the switch matrix, and thus cannot support adequate bypassing.

To address this limitation, the improved equalizer integrates an exclusive gate driver for every switch module within the matrix. This configuration allows the corresponding bypass path to be controlled independently once a faulty cell has been disconnected. Hence, current can be rerouted through specific switches to maintain continuity for the remaining cells, effectively bypassing the failed cell without affecting overall pack operation. Fig. 20 illustrates four representative bypass configurations for a four-cell pack when one cell has been disconnected at different

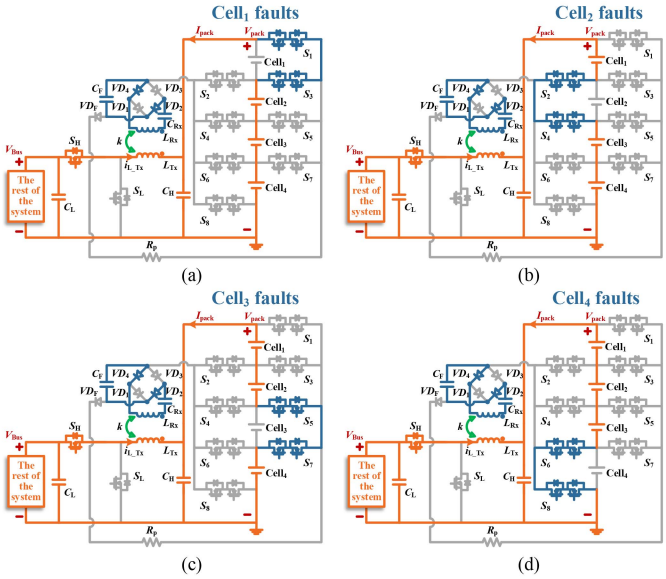

Fig. 20. Bypass configurations for different single-cell fault scenarios in a four-cell battery pack. (a) First cell. (b) Intermediate even-indexed cell. (c) Intermediate odd-indexed cell. (d) Last cell.

TABLE V
SWITCH PAIRS REQUIRED FOR BYPASSING A SINGLE DISCONNECTED CELL

Failed Cell Position	Conducting Switch Pair
First cell ($i = 1$)	S_1 and S_3
Intermediate even-indexed Cell$_i$	S_{2i} and $S_{2(i-1)}$
Intermediate odd-indexed Cell$_i$	S_{2i-1} and S_{2i+1}
Last cell ($i = n$)	S_{2n} and $S_{2(n-1)}$

positions in the string. Moreover, Table V summarizes the switch pairs that need to be conducted for an n-cell string, showing the potential to enhance system robustness under cell-level failure scenarios.

E. Extension for Bidirectional SOC Balancing

In some applications, a power converter may connect to battery packs on both its input and output sides, as in energy storage systems, EVs with auxiliary battery packs, or mobile charging stations. In such cases, simultaneous intrapack SOC balancing at both ends is often required, regardless of whether the packs are charging or discharging. Leveraging the modular design, the presented IPT-based equalizer can be readily extended to meet this demand.

As shown in Fig. 21, the system comprises three functional module types: the pack module, the balancing module, and the converter module. For bidirectional SOC balancing, each pack is equipped with its own balancing module, whose Rx coil is coupled to a large Tx coil in the converter module, enabling effective intrapack balancing on both sides.

At the software level, each pack module computes the SOC of its individual cells and their average value using coulomb counting, then transmits this data to its associated balancing module. Based on the received data, the balancing module regulates the conduction durations of each switch pair to equalize the

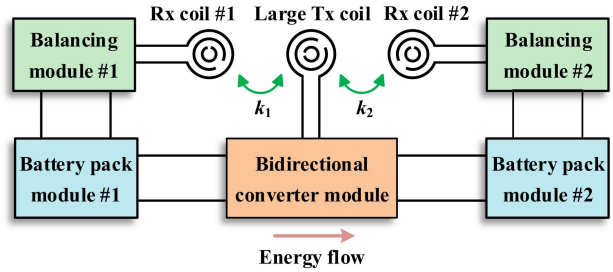

Fig. 21. Modular IPT-based equalizer for bidirectional SOC balancing.

pack. Only minimal SOC data exchange between corresponding modules is required, while the converter module maintains closed-loop control on the output side.

Moreover, the detachable design of the balancing module allows system size to be reduced when balancing is not needed, offering greater flexibility than transformer-based and other WPT/IPT-based equalizers.

F. Discussion on Ferrite Core Material Selection

In this work, a NiZn ferrite core is employed for the Tx coil, following the manufacturer's datasheet of the commercial component. However, at the operating frequency of 200 kHz, MnZn ferrite generally provides better performance than NiZn due to its higher permeability and lower core loss in this frequency range [35], [36].

It should be noted that the primary focus of this work is the balancing topology and SOC equalization control strategy, which are largely independent of the specific ferrite material used. Nevertheless, future work will focus on the influence of magnetic material selection on efficiency, thermal behavior, and system performance to support further improvement and optimization for practical applications.

VI. COMPARISON WITH SIMILAR EXISTING EQUALIZERS

In Table VI, different transformer-, WPT-, and IPT-based battery equalizers are compared in terms of ac power reliance, inverter usage, VM adoption, balancing strategy, and efficiencies in both charging and discharging modes. For some active balancing methods, the BNg indicates the balancing state while the BEd denotes the balanced state. The VMs are incorporated to enhance voltage levels for cell balancing in [21], [22], [23], and [24]. However, this approach inherently introduces conversion losses and increased component stress, leading to relatively low efficiencies of 72.8%–76.8%. In addition, the switch matrix is embedded in the main charging path in [25], resulting in a balancing efficiency of 60.3%. By contrast, in the presented method, the switch matrix is placed in the auxiliary balancing circuit, where the current is relatively low, contributing to only 3.96% of the total power loss and thereby maintaining high overall efficiency.

The work in [18], [19], [20], [21], [22], [23], and [24] benefits from simple control methods, such as automatic or voltage-based control, but these are insufficient for applications requiring high balancing accuracy. In contrast, systems with active and precise

TABLE VI
COMPARISON OF WPT- AND IPT-BASED BATTERY EQUALIZER

Battery Balancing Methods	AC Power Reliance	Inverter Reliance	Voltage Multiplier	Switch Matrix	Balancing Strategy	Control Complexity	Efficiency	
							Charging	Discharging
Transformer-Based Equalizer [18]	No	No	No	No	Automative	Low	94.2%	93.6%
Multiple-Receiver WPT Equalizer [19]	Yes	No	No	No	Automative	Low	74.5%	N/A
Voltage Doubler IPT Equalizer [20]	No	Yes	No	No	Voltage-Based	Moderate	80%	N/A
Scalable Cell-String WPT Equalizer [21]	Yes	No	Yes	No	Automative	Low	76.5%	N/A
Anti-Misalignment WPT Equalizer [22]	No	Yes	Yes	No	Voltage-Based	Middle	76.8%	N/A
Low-Cost WPT Equalizer [23]	Yes	No	Yes	No	Automative	Low	72.8%	N/A
Hybridized Ad-Hoc Wireless Charger [24]	No	Yes	Yes	No	Voltage-Based	Moderate	BNg: 76.4% BEd: 88.6%	N/A
Switch Matrix-Based WPT Equalizer [25]	No	Yes	No	Yes	Voltage-Based	High	BNg: 60.3% BEd: 84.2%	N/A
WPT-Based Modular Equalizer [26]	No	Yes	No	No	Voltage-Based	High	N/A	N/A
WPT Discharging Equalizer [27]	No	No	No	No	SOC-Based	High	N/A	BNg: 68.3% BEd: 87.6%
This Paper	No	No	No	Yes	SOC-Based	Moderate	BNg: 85.8% BEd: 91.5%	BNg: 84.3% BEd: 90.2%

BNg indicates the balancing state, and BEd indicates the balanced state.

TABLE VII
COMPARISON OF COMPONENT COUNTS AND OVERALL COST IN BATTERY EQUALIZERS FOR SIX CELLS (THREE MODULES)

Battery Balancing Methods	Transformer	Diode	MOSFETs	Common source MOSFETs	Switches Driver	Inductor	Capacitor	Coil	Cost
Transformer-Based Equalizer [18]	1	6	2	0	2	0	2	0	$21.8
Multiple-Receiver WPT Equalizer [19]	0	24	5	0	5	3	15	7	$25.3
Voltage Doubler IPT Equalizer [20]	0	6	4	0	4	1	8	4	$28.6
Scalable Cell-String WPT Equalizer [21]	0	12	4	0	4	1	10	4	$30.4
Anti-Misalignment WPT Equalizer [22]	0	18	4	0	4	1	11	5	$36.9
Low-Cost WPT Equalizer [23]	0	12	5	0	5	2	11	2	$22.7
Hybridized Ad-Hoc Wireless Charger [24]	0	12	8	0	8	2	13	2	$26.3
Switch Matrix-Based WPT Equalizer [25]	0	4	12	9	21	1	7	2	$34.0
WPT-Based Modular Equalizer [26]	0	0	24	0	24	6	13	12	$93.9
WPT Discharging Equalizer [27]	0	30	8	0	8	0	15	7	$53.5
This Article	0	4	2	12	8	0	3	2	$21.5

Note: Costs calculated for a quantity of 100 units.

control strategies, such as the switch matrix-based equalizer in [25] and the SOC-based method proposed in this work, achieve higher balancing accuracy at the cost of increased control complexity. It is worth noting that the employed switch matrix features moderate control complexity, as it only adjusts the connection duration of each cell instead of requiring precise real-time current regulation as in [27]. This tradeoff ensures a balance between control simplicity and performance, making it a practical choice for WPT-based battery equalization.

Table VII provides a quantitative comparison of component counts and costs for several six-cell (three-module) equalizer implementations. Key components include multiwinding transformers ($ 18.00 each), diodes ($ 0.20 each), *n*-channel MOSFETs ($ 0.50 each), integrated common-source *n*-channel MOSFETs ($ 0.40 each), drivers ($0.50 each), fixed inductors ($ 1.00 each), capacitors ($ 0.30 each), and coils ($ 5.00 each), all based on pricing for 100-unit orders.

Among these, the presented IPT-based equalizer achieves the lowest total cost of $ 21.50. This cost advantage is attributed to the utilization of a single shared Rx circuit with adaptive connection duration control, enabling accurate SOC balancing while minimizing component count. The integrated common-source MOSFETs further reduce cost by operating under lower voltage and current stresses, allowing the use of lower-rated and more economical devices.

In contrast, transformer-based designs such as [18] are typically custom-designed and require fully symmetrical multiwinding transformers to ensure balancing accuracy, which leads to considerable manufacturing challenges [37]. Therefore, a unit price of $18.00 is reasonably adopted in this comparison, considering the associated customization and manufacturing requirements.

While Xu et al. [18] do not report the volume information, the transformer volume is estimated to be 9.52 cm^3 based on its predecessor work [38] for six cells. This is slightly smaller than the 11.61 cm^3 volume of the coils used in the IPT-based design. However, transformer volume scales with the number of cells, as each cell requires an exclusive secondary winding. In contrast, the Rx coil in IPT-based designs is shared and remains constant regardless of the cell count. Thus, for larger battery systems, the IPT-based equalizer offers not only better cost efficiency but also greater scalability in volume.

VII. Conclusion

In this study, an IPT-based equalizer is presented to achieve efficient battery equalization during both charging and discharging, enhancing its practical applicability. The equalizer utilizes a bidirectional single-inductor dc–dc converter, in which the inductor is replaced by an equivalent impedance Tx coil. A single Rx coil is introduced, wirelessly capturing feedback energy and sequentially connecting to each battery according to a regulated connection duration. Experimental results validate the capability of the presented equalizer to balance the battery pack and confirm the feasibility of the introduced battery balancing controller during both charging and discharging, even under real discharging scenarios and varying coupling coefficients. Furthermore, efficiency analysis reveals significant improvements with the introduced efficient adaptive equalization algorithm, showing a 5.9% gain during discharging and a 5.7% improvement during charging. Moreover, the integration of a switch matrix allows for cell-level fault bypass and mitigates cross-coupling issues within the battery system, thereby significantly enhancing the system's operational reliability and balancing performance.

References

[1] S. Wang, Y. Wang, G. Chen, D. Wei, and Y. Shang, "An efficient and compact equalizer based on forward-flyback conversion for large-scale energy storage systems," *IEEE Trans. Transport. Electrific.*, vol. 10, no. 1, pp. 1222–1232, Mar. 2024.

[2] M. A. Hannan, M. M. Hoque, S. E. Peng, and M. N. Uddin, "Lithium-ion battery charge equalization algorithm for electric vehicle applications," *IEEE Trans. Ind. Appl.*, vol. 53, no. 3, pp. 2541–2549, May 2017.

[3] D. Ansean, M. Gonzalez, V. M. Garcia, J. C. Viera, J. C. Anton, and C. Blanco, "Evaluation of LiFePO4 batteries for electric vehicle applications," *IEEE Trans. Ind. Appl.*, vol. 51, no. 2, pp. 1855–1863, Mar. 2015.

[4] F. Liu, R. Zou, Y. Liu, and Y. Wang, "A modularized voltage equalizer based on phase-shift modulation for series-connected battery strings," *IEEE Trans. Ind. Electron.*, vol. 70, no. 12, pp. 12 475–12 485, Dec. 2023.

[5] M. K. Al-Smadi and J. A. A. Qahouq, "Evaluation of current-mode controller for active battery cells balancing with peak efficiency operation," *IEEE Trans. Power Electron.*, vol. 38, no. 2, pp. 1610–1621, Feb. 2023.

[6] Y. Shang, B. Xia, C. Zhang, N. Cui, J. Yang, and C. C. Mi, "An automatic equalizer based on forward–flyback converter for series-connected battery strings," *IEEE Trans. Ind. Electron.*, vol. 64, no. 7, pp. 5380–5391, Jul. 2017.

[7] N. Ghaeminezhad, Q. Ouyang, X. Hu, G. Xu, and Z. Wang, "Active cell equalization topologies analysis for battery packs: A systematic review," *IEEE Trans. Power Electron.*, vol. 36, no. 8, pp. 9119–9135, Aug. 2021.

[8] W. Liu et al., "Distributed voltage equalization design for supercapacitors using state observer," *IEEE Trans. Ind. Appl.*, vol. 55, no. 1, pp. 620–630, Jan. 2019.

[9] M.-Y. Kim, C.-H. Kim, J.-H. Kim, and G.-W. Moon, "A chain structure of switched capacitor for improved cell balancing speed of lithium-ion batteries," *IEEE Trans. Ind. Electron.*, vol. 61, no. 8, pp. 3989–3999, Aug. 2014.

[10] X. Guo, Q. Wu, C. Xing, W. Qian, and Y. Zhao, "An active equalization method for series-parallel battery pack based on an inductor," *J. Energy Storage*, vol. 64, Aug. 2023, Art. no. 107157.

[11] W. Lujun et al., "Efficient and fast active equalization method for retired battery pack using wide voltage range bidirectional converter and DBSCAN clustering algorithm," *IEEE Trans. Power Electron.*, vol. 37, no. 11, pp. 13 824–13 833, Nov. 2022.

[12] G. Noh, J. Lee, and J.-I. Ha, "Design and analysis of single-inductor power converter for both battery balancing and voltage regulation," *IEEE Trans. Ind. Electron.*, vol. 69, no. 3, pp. 2874–2884, Mar. 2022.

[13] Y. Ye, J. Wang, and X. Wang, "A multi-winding transformer-based active cell equalizer with self-driven switches for series-connected lithium-ion batteries and super-capacitors," *J. Energy Storage*, vol. 703, Oct. 2023, Art. no. 107971.

[14] S. Li, C. C. Mi, and M. Zhang, "A high-efficiency active battery-balancing circuit using multi-winding transformer," *IEEE Trans. Ind. Appl.*, vol. 49, no. 1, pp. 198–207, Jan. 2013.

[15] C.-S. Lim, K.-J. Lee, N.-J. Ku, D.-S. Hyun, and R.-Y. Kim, "A modularized equalization method based on magnetizing energy for a series-connected lithium-ion battery string," *IEEE Trans. Power Electron.*, vol. 29, no. 4, pp. 1791–1799, Apr. 2014.

[16] Y. Shang, N. Cui, and C. Zhang, "An optimized any-cell-to-any cell equalizer based on coupled half-bridge converters for series-connected battery strings," *IEEE Trans. Power Electron.*, vol. 34, no. 9, pp. 8831–8841, Sep. 2019.

[17] Y. Li, J. Xu, X. Mei, and J. Wang, "A unitized multiwinding transformer-based equalization method for series-connected battery strings," *IEEE Trans. Power Electron.*, vol. 34, no. 12, pp. 11981–11989, Dec. 2019.

[18] B. Xu et al., "A double-switch single-transformer integrated equalizer for the recycled power battery string of automatic guided vehicles," *IEEE Trans. Ind. Electron.*, vol. 70, no. 3, pp. 2596–2606, Mar. 2023.

[19] M. Liu, M. Fu, Y. Wang, and C. Ma, "Battery cell equalization via megahertz multiple-receiver wireless power transfer," *IEEE Trans. Power Electron.*, vol. 33, no. 5, pp. 4135–4144, May 2018.

[20] L. Liu et al., "A multiple-receiver-IPT-based voltage equalizer with voltage doublers for battery-string charging," in *IEEE J. Emerg. Sel. Top. Power Electron.*, vol. 13, no. 1, pp. 1339–1348, Feb. 2025.

[21] P. Zhang et al., "Wireless power transfer-based voltage equalizer for scalable cell-string charging," *IEEE Trans. Ind. Electron.*, vol. 71, no. 1, pp. 493–503, Jan. 2024.

[22] P. Zhang et al., "Dual-layer equalization architecture for anti-misalignment capability enhancement in multiple-receiver-based WPT equalizer," *IEEE Trans. Power Electron.*, vol. 39, no. 10, pp. 14027–14038, Oct. 2024.

[23] M. Fu, C. Zhao, J. Song, and C. Ma, "A low-cost voltage equalizer based on wireless power transfer and a voltage multiplier," *IEEE Trans. Ind. Electron.*, vol. 65, no. 7, pp. 5487–5496, Jul. 2018.

[24] P. Zhang et al., "Wireless charging of large-scale energy storage systems: A hybridized ad-hoc approach for high efficiency," *IEEE Trans. Power Electron.*, vol. 38, no. 11, pp. 13 374–13 383, Nov. 2023.

[25] J. Sun et al., "A novel charging and active balancing system based on wireless power transfer for lithium-ion battery pack," *J. Energy Storage*, vol. 55, 2022, Art. no. 105741.

[26] D. Zheng et al., "Research on battery module equalization strategy for wireless power transfer system," in *Proc. Int. Conf. Power Energy Syst. Appl.*, 2023, pp. 139–143.

[27] Y. Cao, Y. Liao, L. Chen, C. Wang, and Y. Hu, "A wireless power feedback-based battery equalizer with multiple-receiver," *IEEE Trans. Transp. Electrif.*, vol. 11, no. 4, pp. 9332–9345, Aug. 2025.

[28] X. He, C. Zhu, J. Tao, Y. Zhang, and R. Mai, "Analysis and design of a cost-effective WPT system with single-input and multioutput based on buck-integrated rectifier," *IEEE Trans. Power Electron.*, vol. 38, no. 10, pp. 12 388–12 393, Oct. 2023.

[29] M. Uno and K. Tanaka, "Single-switch multioutput charger using voltage multiplier for series-connected lithium-ion battery/supercapacitor equalization," *IEEE Trans. Ind. Electron.*, vol. 60, no. 8, pp. 3227–3239, Aug. 2013.

[30] Y. Cao and J. A. Abu Qahouq, "Analysis and evaluation of a dual-variable closed-loop control of power converter with wireless and nonwireless power transfer," *IEEE Trans. Ind. Electron.*, vol. 66, no. 4, pp. 2668–2679, Apr. 2019.

[31] C. Wang, R. Li, Y. Cao, and M. Li, "A hybrid model for state of charge estimation of lithium-ion batteries utilizing improved adaptive extended Kalman filter and long short-term memory neural network," *J. Power Sources*, vol. 620, Nov. 2024, Art. no. 235272.

[32] C. Wang, F. Li, Y. Liao, and Y. Cao, "Flyback converter based charge balancing control with cell-load and cell-cell operation modes in battery system," *Appl. Energy*, vol. 394, Sep. 2025, Art. no. 126181.

[33] X. Cui, W. Shen, Y. Zhang, C. Hu, and J. Zheng, "Novel active LiFePO4 battery balancing method based on chargeable and dischargeable capacity," *Comput. Chem. Eng.*, vol. 97, pp. 27–35, Feb. 2017.

[34] Y. Wang, C. Zhang, Z. Chen, J. Xie, and X. Zhang, "A novel active equalization method for lithium-ion batteries in electric vehicles," *Appl. Energy*, vol. 145, pp. 36–42, May 2015.

[35] Z. Li et al., "Microstructure, magnetic properties, and loss performance of the Cu-substituted MnZn ferrites," *Ceram. Int.*, vol. 49, no. 24, pp. 40275–40283, Dec. 2023.

[36] P. Andalib and V. G. Harris, "Grain boundary engineering of power inductor cores for MHz applications," *J. Alloys Compd.*, vol. 832, Aug. 2020, Art. no. 153131.
[37] W. Huang and J. A. A. Qahouq, "Energy sharing control scheme for State-of-charge balancing of distributed battery Energy storage system," *IEEE Trans. Ind. Electron.*, vol. 62, no. 5, pp. 2764–2776, May 2015.
[38] L. Liu et al., "A low-cost multiwinding transformer balancing topology for retired series-connected battery string," *IEEE Trans. Power Electron.*, vol. 36, no. 5, pp. 4931–4936, May 2021.

Yinqin Liao (Student Member, IEEE) was born in Hunan, China, in 2002. He received the B.S. degree in electrical engineering and automation from Ningxia University, Yinchuan, China, in 2023. He is currently working toward the M.S. degree in electrical engineering with Central South University, Changsha, China.

His current research interests include battery management systems, wireless power transfer systems, and hybrid energy systems.

Xinzhi Zhang was born in Hunan, China, in 2003. He received the B.S. degree in electrical engineering and automation from Wuhan Institute of Technology, Wuhan, China, in 2024. He is currently working toward the M.S. degree in electrical engineering with Central South University, Changsha, China

His current research interests include SOH estimation and consistency evaluation of battery in terms of deep learning and AI.

Long Chen (Student Member, IEEE) was born in Anhui, China, in 2002. He received the B.S. degree in electrical engineering, in 2023, from Central South University, Changsha, China, where he is currently working toward the M.S. degree in electrical engineering.

His research interests include battery management systems and renewable energy systems.

Feiliang Li was born in Jiangxi, China, in 2000. He received the B.S. degree in electrical engineering, in 2021, from Central South University, Changsha, China, where he is currently working toward the Ph.D. degree in electrical engineering

His current research interests include battery management systems, wireless power transfer systems, and hybrid energy systems.

Chunsheng Wang (Member, IEEE) received the B.S. degree in engineering from Beijing Jiaotong University (formerly known as Northern Jiaotong University), Beijing, China, in 1991, the M.S. degree in engineering from Southwest Jiaotong University, Chengdu, China, in 2004, and the Ph.D. degree in engineering from Central South University, Changsha, China, in 2008

In 2008, he joined as the Staff with Central South University, where he is currently a Professor with the School of Automation. His current research interests include optimization and control of multicarrier energy network modeling, energy management and integrated energy systems, and artificial intelligence and applications.

Yuan Cao (Member, IEEE) received the B.S. and M.S. degrees from Central South University, Changsha, China, in 2011 and 2014, respectively, and the Ph.D. degree from the Department of Electrical and Computer Engineering, The University of Alabama, Tuscaloosa, AL, USA, in 2019, all in electrical engineering

He is currently an Associate Professor with the School of Automation, Central South University. Prior to this, he was employed with Baidu USA, Sunnyvale, CA, USA, and Hyperloop, Los Angeles, CA, USA, as a Senior Electrical Engineer. His research interests include energy storage, battery management systems, and wireless power transfer systems.

Dr. Cao was the recipient of the Graduate Council Fellowship Award, in 2015 and 2017, respectively. He was also the recipient of the outstanding student award from the College of Engineering, the University of Alabama, in 2018 and 2019.

Yukun Hu (Senior Member, IEEE) received the Ph.D. degree in chemical engineering from the Royal Institute of Technology (KTH), Stockholm, Sweden, in February 2013

He is currently an Associate Professor of Infrastructure Systems with the Department of Civil, Environment and Geomatics Engineering, University College London (UCL) and a member of the UCL's Infrastructure Systems Institute, where he leads the energy theme research. His research interests include the development of advanced modeling, control, and optimization methods in the field of energy processes. He has experience in a wide range of modeling methods, such as molecular dynamics, process simulation, computational fluid dynamics, zone modeling, agent-based modeling, and artificial intelligence techniques, including neural networks and genetic algorithms.